

DEVELOPMENT OF AN INTRAOPERATIVE GAMMA CAMERA BASED ON A 256-PIXEL MERCURIC IODIDE DETECTOR ARRAY

Bradley E. Patt, *Member, IEEE*, Martin P. Tornai*, *Student Member, IEEE*, Jan S. Iwanczyk, *Member, IEEE*, Craig S. Levin*, *Member, IEEE*, and Edward J. Hoffman*, *Senior Member, IEEE*

Advanced Detectors Inc., 1220-A Avenida Acaso, Camarillo, CA 93012

** Division of Nuclear Medicine & Biophysics, Department of Molecular & Medical Pharmacology, UCLA School of Medicine, Los Angeles, CA 90095*

ABSTRACT

A 256-element mercuric iodide (HgI_2) detector array has been developed which is intended for use as an intraoperative gamma camera (IOGC). The camera is specifically designed for use in imaging gamma-emitting radiopharmaceuticals (such as $^{99\text{m}}\text{Tc}$ labeled Sestamibi) incorporated into brain tumors in the intraoperative surgical environment. The system is intended to improve the success of tumor removal surgeries by allowing more complete removal of subclinical tumor cells without removal of excessive normal tissue. The use of HgI_2 detector arrays in this application facilitates construction of an imaging head that is very compact and has a high SNR. The detector is configured as a cross-grid array. Pixel dimensions are 1.25 mm squares separated by 0.25 mm. The overall dimension of the detector is 23.75 mm on a side. The detector thickness is 1 mm which corresponds to over 60% stopping at 140 keV. The array has good uniformity with average energy resolution of $5.2 \pm 2.9\%$ FWHM at 140 keV (best resolution was 1.9% FWHM). Response uniformity ($\pm \sigma$) was 7.9%. A study utilizing realistic tumor phantoms (uptake ratio varied from 2:1 to 100:1) in background (1 mCi/l) was conducted. SNR's for the reasonably achievable uptake ratio of 50:1 were 5.61σ with 1 cm of background depth ("normal tissue") and 2.74σ with 4 cm of background for a 6.3 μl tumor phantom (~ 270 nCi at the time of the measurement).

I. INTRODUCTION

The success of surgical intervention for brain tumor patients depends on the extent to which the surgeon is able to remove all of the viable tumor cells from the patient [1-3]. Characterization of the lesion preceding neurosurgery by preoperative radiological imaging studies (CT and/or MRI) is an essential part of the local staging of the primary tumor. The images thus produced provide the surgeon with a static localization of the neoplasm.

However, these modern 3-D neuro-imaging techniques have some difficulty in differentiating tumor from the surrounding edema due to the altered blood-brain barrier. Even with stereotactical surgery systems, the changes in the geometry of the brain that often occur intraoperatively due to

edema, ventricular drainage and maneuvers to dehydrate the brain (e.g., use of hyperventilation and osmotic agents) can invalidate the preoperative measurements. In addition intraoperative ultrasound will frequently miss infiltrative cells at the margin of the tumor. While these procedures have

importance in the preoperative staging of the tumor, more sensitive and effective methods of tumor localization are required. Although imaging systems to detect beta-radiation are under investigation to identify the fringes of the tumor [4,5] there are no imaging tools currently available to the surgeon for intraoperative localization of subclinical tumoral mass remaining after the surgeon has extricated the obviously tumorous tissue.

Thus while the body of the tumor, which may be grossly necrotic, hemorrhagic or otherwise obvious to the surgeon, can usually be identified easily and removed, the margins and extensions of the tumor in normal tissue are very difficult to locate and identify. In many cases tissue samples may be biopsied to check if tumor cells are present, but this process is painstaking, typically undersamples the tissue bed, and is extraordinarily time consuming.

Recent developments, in the testing of radiopharmaceuticals (such as $^{99\text{m}}\text{Tc}$ labeled Sestamibi), have shown that these compounds are selectively taken up in tumors, apparently in proportion to the malignancy of the tumor [6-10]. This provides a mechanism for intraoperatively "tagging" tumor and differentiating it from normal tissue. The patient is injected with a tumor seeking radiopharmaceutical before surgery, the surgical procedure to remove the tumor mass is performed, and the site is then imaged using the IOGC probe to locate residual subclinical tumor cells.

A small, light weight, high-resolution intraoperative gamma-camera (IOGC) capable of imaging the distribution of the radiopharmaceutical in the surgical environment has a number of unique and enabling applications in tumor detection and in tumor surgery, by enabling the neurosurgeon to remove more of the viable tumor cells from the patient with a cerebral neoplasm without removing normal cerebral tissue that is supporting vital functions. An additional motivation for developing an imaging probe comes from the literature citing the success achieved with non-imaging intraoperative probes [11-14]. In most of the applications reported, an IOGC would be much more sensitive and effective in dealing with the tumor localization problem.

II. DETECTOR DESIGN AND OPTIMIZATION

Our work has focused on investigating the feasibility of developing a small area HgI_2 detector array with design optimized for intraoperative surgical procedures. Advantages of HgI_2 are that it does not need cryogenic cooling and is

superior to all scintillator and gas based systems due to its excellent signal-to-noise ratio (SNR). The HgI_2 detector allows the necessary miniaturization required to optimize the construction of a device to operate proximal to the tissue in the surgical field. Close proximity results in improved sensitivity, spatial resolution, and contrast.

In our previously reported work [15,16] we conducted an investigation to determine the optimal construction of the probe front end including the detector and front-end electronics. These efforts were confirmed through the construction and evaluation of prototypical nineteen element arrays. Several new and novel developments which resulted from the early investigations and which were responsible for significant improvements in device performance have been implemented in the current work.

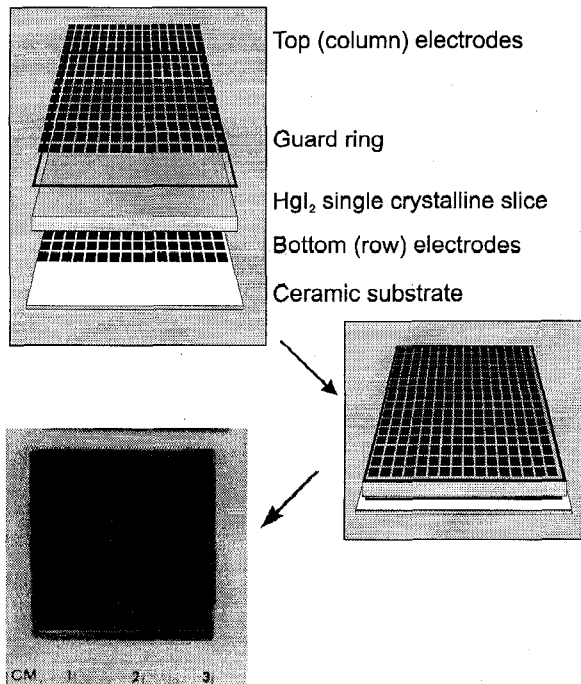


Figure 1. Illustration of the mercuric iodide array design. Electrodes and guard ring structures are constructed on the HgI_2 crystalline faces via evaporation of Pd through a physical mask. The top electrode consists of individual Pd. Pads joined together using 1 mil. Pd wires along columns. The bottom electrode has individual pixel pads arranged to form rows. The detector is adhered to a ceramic substrate. A digitized photograph of the 256-pixel array is shown at bottom-left in the figure.

A novel discrete-pixel electrode patterning with adjacent elements joined by thin wires (as opposed to previously employed parallel-line cross-grid arrays) and guard rings have helped to improve the electric field distribution, and hence improve the charge collection [15]. The array design incorporates a pseudo cross-grid array structure. The array construction and a photograph of the 256-pixel detector are shown in Figure 1. The pseudo cross-grid array configuration used for the detector has orthogonal sets of electrodes: (rows and columns), on the front and back sides of the device respectively. Signals from both sides of the detector are used

for the spatial information, and only the signals from the lower-noise back-side of the detector (rows) are used for the spectroscopic information.

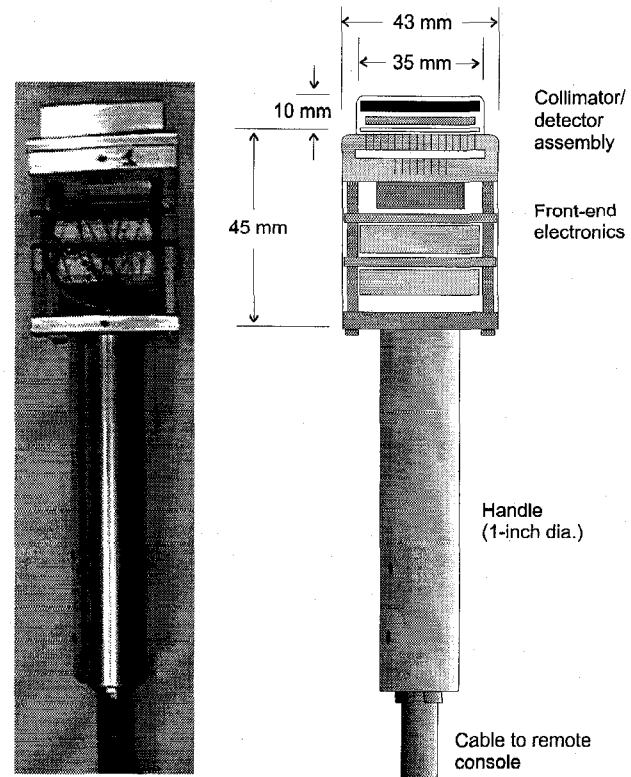


Figure 2. Digitized photograph (left) and sketch of the probe (right). The probe housing contains the collimator, HgI_2 detector array, front-end FET's, and coupling to the preamplifiers. A variation of the handle is planned to accommodate miniaturized preamplifiers and a DC-DC converter for the detector bias.

We have taken into account the technological issues of detector fabrication, the major requirements for subclinical tumor localization including spatial resolution, spectral performance, efficiency, expected count rates, and clinical constraints on the size of the probe. Based upon these considerations pixel dimensions were chosen to be 1.25 mm squares separated by 0.25 mm. The overall dimension of the detector is 23.75 mm on a side. The detector thickness is > 1 mm (corresponding to over 60% stopping at 140 keV).

Tungsten collimators with square holes matching the pixel geometry (1.25 mm squares) and septal wall thickness matching the inter-element spacings (0.25 mm) were fabricated. Modular segments of the collimator can be arranged to form collimator thicknesses from 2 mm up to 2 cm. The collimators are adhered to the detector surface.

We have currently completed the design, fabrication and initial evaluation of the 256-pixel detector. Processing electronics, data collection hardware and software are also currently being finalized. To date we have assembled the necessary number of electronic modules to allow testing of 10 by 10 (100-element) sections of the 256-element array.

A photograph and sketch of the probe is shown in Figure 2. The front end containing the collimator/ detector assembly (with matched collimator-hole cross section and detector

element dimensions) and front-end electronics (first stage FET's and associated structures) are highly miniaturized so that all of these components will fit within an assembly with a ~ 4 cm outside dimension as shown. Additional aligned collimator segments can be accommodated with the use of small alignment pins built into the cover. A DC-DC converter and miniaturized preamplification electronics could be built into a modified handle, slightly larger than the present one, but constrained to be of a suitable size to be comfortably held in the surgeons hand. The probe attaches to a remote console for data acquisition, image processing and display.

III. DETECTOR CHARACTERIZATION

A. Equipment

Detector Test Chamber

A test chamber was designed and constructed for testing the various components ("raw" detector assemblies, and input electronics) of the IOGC under development. The chamber consists of two housings: 1) A detector housing which accommodates the front-end components (detector, FET's and other front-end electronics) for arrays up to 32 by 32 (1024 pixels); and 2) A preamplifier housing which accommodates the preamplifiers.

Signals from the detector housing are fed to the preamplifier housing. Each row and column electrode from the cross-grid detector array is coupled to a charge sensitive preamplifier. The preamplifiers are a low noise circuit which was designed for the IOGC using a combination of surface mount and full-size discrete components. The preamplifiers will eventually be housed in the probe assembly. Noise characteristics were measured to be $< 40 e^-$ RMS for the spectroscopy entire front end with the detector fully biased.

Data Acquisition System

Detector characterization and imaging measurements were made with the low noise IOGC preamplifiers coupled to Advanced Detectors CAMAC based programmable shaping amplifiers with programmable gain and shaping time selection of 14 μ s or 2.4 μ s. Digital outputs were provided from each channel for signals exceeding a specified threshold set just above the noise. Analog signals (with the 14 μ s triangular shaping time, and individually balanced gains) from each channel (row and column) were digitized with a peak sensing Phillips CAMAC based ADC (16 channel 7164). Gating for the ADC was provided by a logic signal produced by "OR"ing the digital outputs of the amplifiers for the "row" signals. The data acquisition and control utilized LabVIEW™ (national Instruments) on a 150 MHz Pentium based PC (Gateway).

Imaging times were limited by the data acquisition system which was count rate limited to about 100 cps, whereas the expected count rates for intraoperative tumor imaging are expected to be between 100 cps and 1000 cps over the detector area. On the other hand, the intrinsic count rate of the

HgI₂ device given the parallel system described above is ~14 kcps per pixel (at 28 μ s and up >50k cps at 4 μ s).

B. Measurements

Characterization of the Uncollimated Detector

The uniformity of a 10 by 10 section of the uncollimated 16 by 16 device was characterized by measuring the response to uniform irradiation of the detector with ⁵⁷Co (122 keV and 136 keV photopeaks). Uniformity ($\pm \sigma$ %) which is defined as the variation in the counts per pixel over the entire imaging field of view, was 6.3 % for full spectral window. The average pixel resolution was 5.3 ± 2.6 % FWHM.

A two source measurement was made simultaneously with ²⁴¹Am and ⁵⁷Co point sources 2.2 cm from the detector array. An 2 mm diameter Pb pinhole collimator was placed between the sources and the exposed detector array allowing the point sources to project onto the detector surface. By simple windowing on either the 59 keV ²⁴¹Am or the 122 keV ⁵⁷Co photopeaks either point projection could be clearly visualized. This dual source capability can be useful during a surgical procedure which uses a radiotracer of one energy and surgical instruments with a radioisotope of another energy embedded onto the tip(s) of the instruments. Thus, the working end of the surgical instruments could be simultaneously visualized (in a different color for example) while the surgeon scans the tissue bed for residual tumor with the imaging device.

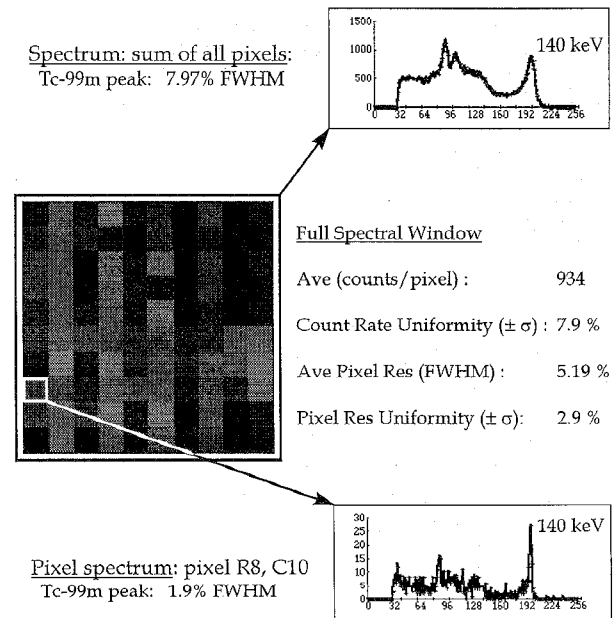


Figure 3. Response of 10 by 10 section of the 16 by 16 array collimated using a 5 mm thick tungsten collimator to uniform irradiation with ⁵⁷Co.

Characterization of the Collimated Detector

Images obtained with a 10 by 10 section of the 16 by 16 device collimated using a 5 mm thick tungsten collimator (Thermo Electron, Tecomet Division) with holes matched to

the detector pixels are shown in Fig's. 3 and 4. Figure 3 shows the response to uniform irradiation of the detector with ^{99m}Tc (140 keV photopeak). Uniformity ($\pm \sigma$ %) is 7.9 % for the full spectral window. The average pixel resolution was 5.2 ± 2.9 % FWHM. The pixel spectrum (resolution is 1.9 % FWHM) is also shown for the best pixel as indicated.

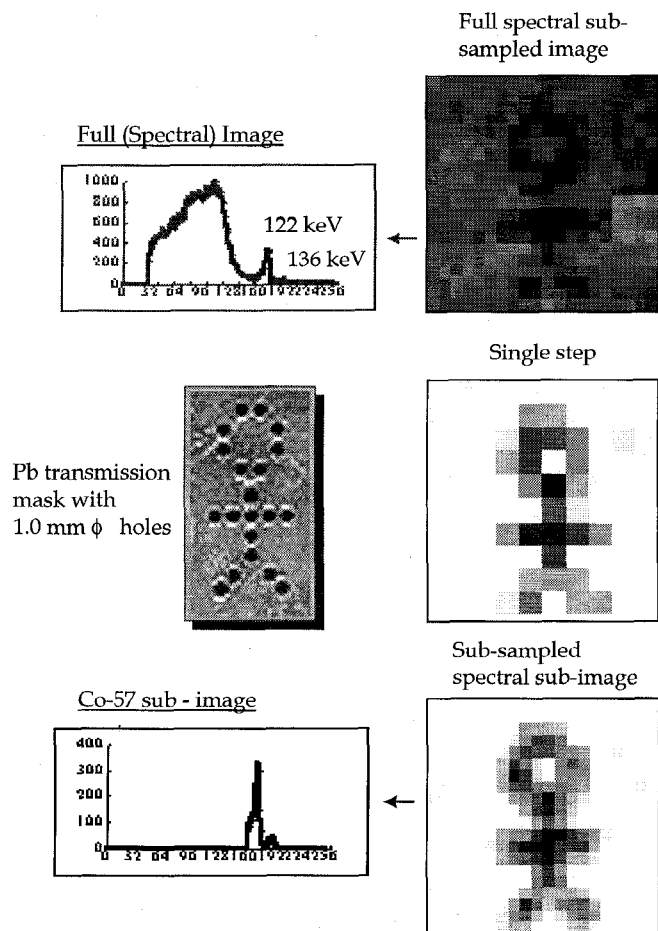


Figure 4. Shadow images of a lead mask with "stick-man" shaped aperture. The configuration of the mask is shown at center left. Holes are 1.0 mm diameter with 1.4 mm spacings. The image at top right is a sub-sampled full-energy spectrum composite of four interleaved single-step images acquired at half-pixel spacings. The corresponding energy spectrum is shown at top left. The image at bottom right is a sub-sampled energy-windowed composite. The corresponding spectrum is shown at bottom left. Center right is a single-step energy windowed image.

Figure 4 shows the shadow images of a lead mask with an "stick-man" shaped aperture. The configuration of the mask is shown at the center-left of the figure. The images were obtained with a ^{57}Co source. The image at top-right is a sub-sampled full-energy spectrum composite image obtained by interleaving four single-step images acquired at half-pixel spacings. The image contains a large degree of scattering from the aperture and other media as can be seen in the energy spectrum shown at top left. At center-right is one of the single-step images making up the composite following spectral

windowing to reduce the scatter. The effect of photopeak windowing and the advantage of the good energy resolution capabilities of the mercuric iodide detector for scatter rejection is shown in the sub-sampled energy-windowed composite image at bottom-right where windowing about the ^{57}Co 122 keV photopeak has eliminated a large portion of the scatter. The corresponding energy spectrum is shown at bottom-left.

Measurement of the Line Spread Function

The line spread function (LSF) response was measured using a 0.7 mm I.D. (1.25 mm O.D.) needle filled with ^{99m}Tc (0.25 mCi/mL). The "line" was stepped in 0.2 mm increments horizontally along the detector. The measured LSF data and gaussian fits to the data are shown in Fig. 5. The LSF was compared with the theoretical response obtained by convolution of a rectangular detector response (1.25 mm) with a rectangular source function (0.7 mm). The measured spatial response was 1.59 mm FWHM resolution with centroid spacing of 1.39 mm compared with theoretical prediction of 1.6 mm FWHM resolution and 1.5 mm centroid spacing.

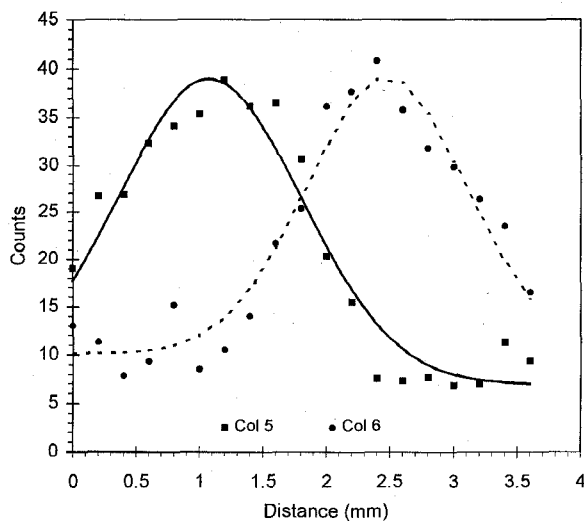


Figure 5. Line spread function response measured by stepping a 0.7 mm line in 0.2 mm increments horizontally along the collimator. Response for two adjacent columns is shown.

Tumor Phantom Study

A study utilizing realistic tumor phantoms in "normal-tissue" background with uptake activity concentration ratio varied from 2:1 to 100:1 was conducted. We used ^{99m}Tc activity concentration of 1 mCi/l for the "normal tissue" based on reported data for ^{99m}Tc Sestamibi uptake in the brain [8]. Such activity concentrations were achieved with 10 - 20 mCi doses. In the study, images were taken for each of three tumor phantoms, (a) 2mm ϕ by 2mm (h) (6.3 μl); (b) 3mm ϕ by 4.1mm (h) (16 μl); and (c) 6mm ϕ by 5.2mm (h) (114 μl). The setup used to acquire the images is shown in Fig. 6. The tumor phantom was always placed on the surface of the detector simulating surface (as opposed to buried) subclinical tumors, and it was always located in the center of the detector.

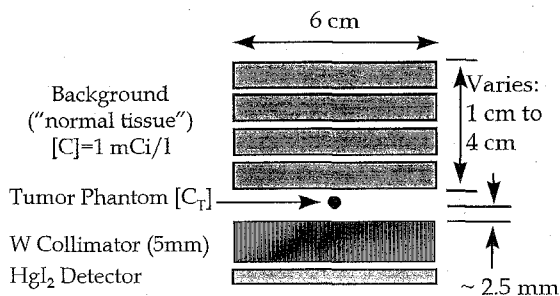


Figure 6. Physical setup used for the tumor phantom study.

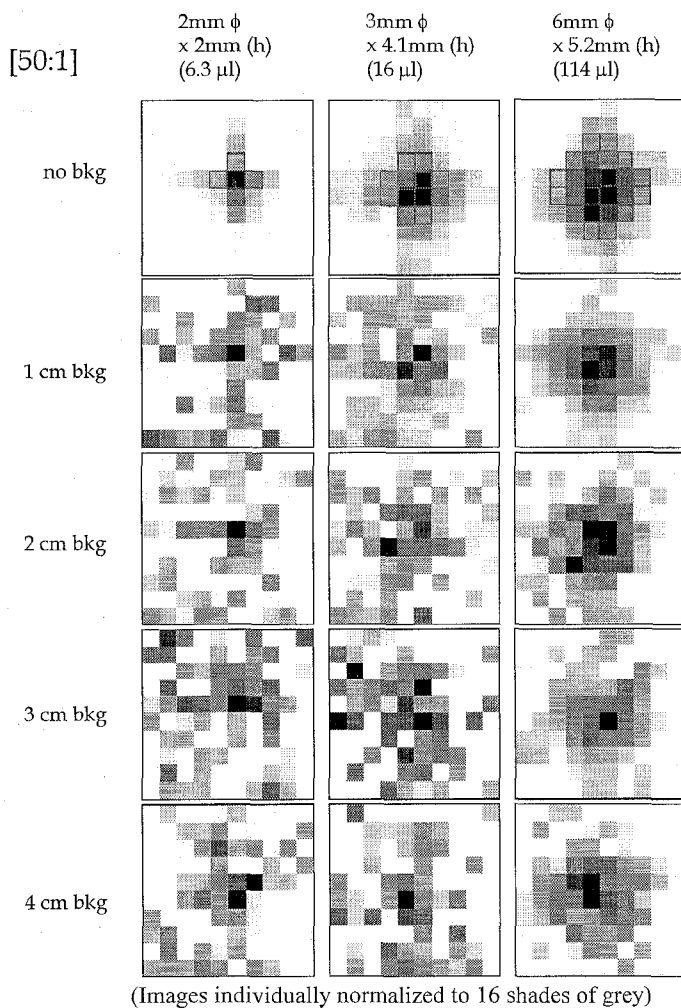
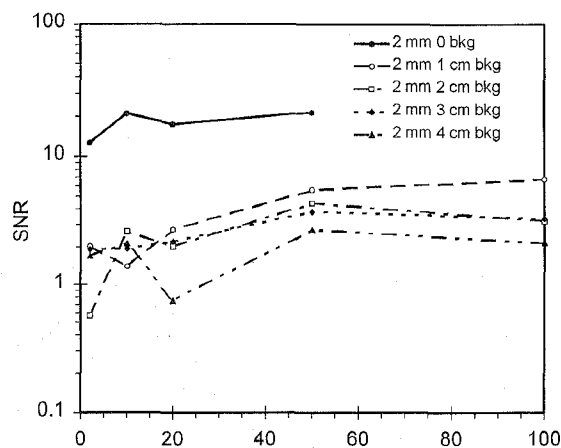


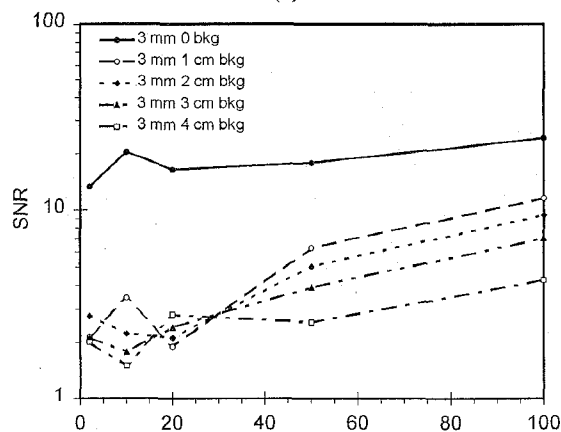
Figure 7. Images of each of the tumor phantom volumes (6.3 µl left column; 16 µl center column; and 114 µl right column) as a function of varying normal-tissue phantom depth behind the tumor (rows) for 50:1 tumor/normal-tissue activity concentration ratio. Regions of interest for the analysis described in the text are drawn over the background data. The greyscale for each image has been individually normalized to 16 shades.

The amount of “normal tissue” beneath the tumor was simulated by varying the number of 1cm thick disks (0; 1cm, 2cm; 3cm; and 4cm total thicknesses were employed) each with the same “normal tissue” activity concentration of ~ 1mCi/L. Images were collected for each of the three tumor volumes and each of the five backgrounds for 10 minutes each.

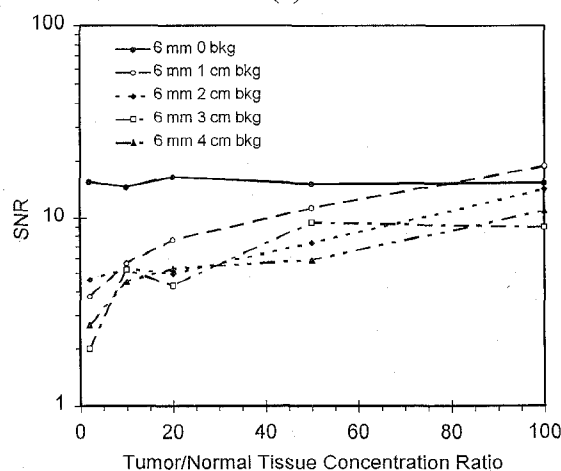
The detector was collimated using the 5 mm thick tungsten collimator.



(a)



(b)



(c)

Figure 8. Measured SNR for (a) 2mm ϕ by 2mm (h) (6.3 µl); (b) 3mm ϕ by 4.1mm (h) (16 µl); and (c) 6mm ϕ by 5.2mm (h) (114 µl) tumor phantoms as a function of tumor to normal tissue activity concentration ratio. Individual curves are 0; 1cm, 2 cm; 3 cm; and 4 cm of normal tissue thicknesses behind the tumors.

Fig. 7 shows the resulting images for each of the tumor volumes as a function of the background for the 50:1 tumor to "normal tissue" concentration ratio. Regions of interest (ROI) for subsequent calculations are drawn around the tumor with the zero background concentration. All images (such as in Fig. 7) were processed by subtracting the average pixel value outside of the ROI from the entire image.

The measured SNR for the various tumor phantoms are shown in Fig. 8 as a function of tumor to normal tissue activity concentration ratio. Individual curves are for 0; 1 cm, 2 cm; 3 cm; and 4 cm of backgrounds behind the tumors. SNR is defined as the ratio of the background corrected peak counts within the a priori known region of interest divided by the standard deviation of the pixel counts in the image outside of the region of interest. From Fig. 8 we see for example that by setting a threshold for detection of 3σ (99.7% confidence level assuming normally distributed noise) the 2 mm ϕ tumor is detected at tumor to normal tissue concentration ratio above about 40 for 3 cm thick or less of normal tissue behind the tumor. The 2 mm ϕ tumor can never be detected with this confidence level in 4 cm thick or more of normal tissue with 10 minutes of acquisition. The 3 mm ϕ tumor can be seen in up to 3cm normal tissue at uptake ratio of 35, and in 4 cm of normal tissue for uptake ratios above 70. The 6 mm ϕ tumor can be easily detected at this confidence level in 10 minutes for uptake ratios of 8 and above.

SNR's for reasonably achievable uptake ratio of 50:1 [10] of 5.61σ with 1 cm of background depth ("normal tissue") and σ with 4 cm of background were obtained for a $6.3\ \mu\text{l}$ tumor phantom ($\sim 270\ \text{nCi}$ at the time of the measurement).

IV. CONCLUSIONS

A 256-element mercuric iodide (HgI_2) detector array has been developed for use as an intraoperative gamma camera (IOGC). The detector has been optimized specifically for use in imaging gamma-emitting radiopharmaceuticals (such as $^{99\text{m}}\text{Tc}$ labeled Sestamibi) incorporated into brain tumors in the intraoperative surgical environment. The use of HgI_2 detector arrays in this application facilitates construction of an imaging head that is very compact and has a high SNR. The detector is configured as a cross-grid array. Pixel dimensions are 1.25 mm squares separated by 0.25 mm. The overall dimension of the detector is 23.75 mm on a side. The detector thickness is 1 mm which corresponds to over 60% stopping at 140 keV. A 10 by 10 segment of the 256-pixel array was characterized using a specially constructed detector chamber with low-noise electronics ($< 40\ \text{e RMS}$) for spectroscopy.

Excellent energy resolution was measured for the 100 uncollimated active pixels in the imaging array, with a high degree of uniformity ($5.3 \pm 2.6\%$ FWHM at 122 keV). With the 5 mm tungsten collimator attached, there was no degradation in the energy resolution ($5.2 \pm 2.9\%$ FWHM at 140 keV). The best single pixel energy resolution was 1.9 % FWHM at 140 keV, which along with the high degree of resolution uniformity demonstrates the high SNR that can be

achieved with the pixellated cross-grid array design. This level of SNR will be especially useful as an excellent means of scatter rejection 'in situ', as demonstrated by rejection of scatter in the Pb transmission phantom imaging experiments. The high degree of uniformity for the large number of pixels will also ensure compliance with NEMA acceptance and operating criteria.

The line spread function response was initially characterized for the collimated imaging system. The measured spatial resolution with the line source in air corresponded to the theoretical values (1.59 mm and 1.60 mm FWHM, respectively), and the centroid spacing of the LSFs corresponded to the detector pitch (1.39 mm and 1.50 mm, respectively). The intrinsic resolution of the detector system, however, is defined by the pixel size of 1.25 mm. These results validate that intrinsic spatial resolution is determined by the pixellation in the array imaging system, and also demonstrate the ability to scale up the imaging array from the smaller initial 19-element array prototype initially developed [15,16].

Several studies characterized the intrinsic properties of the array with the operational 100-element segment of the 256-element imaging array. Further studies were undertaken to understand some limitations of the application of the array for real-time intraoperative imaging. The 10 min imaging times were limited by the hardware count rate limitation of the data acquisition system. Future optimization of the system by employing intelligent crate controllers with more local processing can remove this limitation.

Nonetheless, realistic tumor phantoms with activity concentrations ratios (equivalent to tumor uptake ratios) from 2:1 to 100:1 tumor:background were conducted. With 50:1 concentration ratios in a $6.3\ \mu\text{l}$ tumor phantom (270 nCi activity at time of measurement), the SNR's decreased from 5.61σ to 2.74σ with increasing background thicknesses from 1 to 4 cm. Thus, based on the minimum SNR (2.74σ) with this concentration ratio, a $6.3\ \mu\text{l}$ (2 mm diameter) tumor can be visualized with 99.4% confidence and 100% sensitivity. For different concentration ratios these values differ, however, 50:1 uptake is not unrealistic based on measured results with currently available radiotracers [10]. These results are very encouraging for 'in situ' residual tumor imaging in the brain and perhaps other organs such as the thyroid and breast that have also demonstrated high uptake of radiotracer with low backgrounds, and also with developments in newer radiopharmaceuticals with potentially higher tumor affinity, e.g. monoclonal antibodies.

The HgI_2 intraoperative imaging device developed in this work has demonstrated high imaging resolution combined with excellent scatter rejection for nuclear emission imaging of clinical radiotracers. These factors, along with the demonstrated ability to visualize very small tumors from background with realistic uptake ratios illustrate the effectiveness of 'in situ' imaging as an aid for remnant tumor detection and localization. The clinical utility of these devices

on positive post-surgical patient outcome must now be validated.

ACKNOWLEDGMENTS

The authors would like to acknowledge the technical assistance of Mrs. F. Riquelme, Mrs. X. Qin, Mr. J. Menjivar, Mr. R. Koziol, Mr. G. Maculewicz, and Mr. R. Szczebiot. The authors gratefully acknowledge the support of this work by the National Institutes of Health under NCI-SBIR Grant No's: 2R44CA61403, 1R43CA68845 and 1R43CA69988.

REFERENCES

- [1] Black, S. Ronner, "Cortical Mapping for Defining the Limits of Tumor Resection," *Neurosurgery*, Vol. 20, pp. 914-919, 1987.
- [2] M.J. Winger et al, "Supratentorial Anaplastic Gliomas in Adults: The Prognostic Importance of Extent of Resection and Prior Low Grade Glioma," *J. Neurosurg.* Vol. 71 (1989) 487-493.
- [3] Nazarro, E. Neuwelt, "The Role of Neurosurgery in the Management of Supratentorial Intermediate and High-Grade Astrocytomas in Adults." *J. Neurosurg*, Vol. 73, pp. 331-344, 1990.
- [4] L. R. MacDonald et al, "Small Area Fiber Optic Coupled Scintillation Camera for Imaging Beta-Ray Distributions Intraoperatively," *Proc SPIE: Photoelectronic Detectors, Cameras and Systems*. Vol 2551 (1995) 92-101.
- [5] M.P. Tornai et al, "Design Considerations and Initial Performance of 1.2 cm² Beta Imaging Intraoperative Probe," *IEEE Trans. Nucl. Sci.*, Vol 43, No. 4 (1996) 2326 - 2335.
- [6] Park CH; Kim SM; Zhang J; McEwan JR; Intenzo C. Tc-99m MIBI brain SPECT of an acoustic schwannoma. *Clin. Nucl. Med.*, 1994 Feb, 19(2):152-4.
- [7] Park CH; Kim SM; Zhang JJ; Intenzo CM; McEwan JR. Tc-99m MIBI brain SPECT in the diagnosis of recurrent glioma. *Clin. Nucl. Med.*, 1994 Jan, 19(1):57-8.
- [8] Maublant JC; Zhang Z; Rapp M; Ollier M; Michelot J; Veyre A. In vitro uptake of technetium 99m-teboroxime in carcinoma cell lines and normal cells: comparison with technetium-99m-sestamibi and thallium-201. *J. Nucl. Med.*, 1993 Nov, 34(11):1949-52.
- [9] Packard AB; Kronauge JF; Limpa-Amara N; Lampson L; O'Tuama LA; Jones AG. Tumor uptake of 99mTc-MIBI and 201Tl by a 9L gliosarcoma brain tumor model in rats. *Nucl. Med. & Biol.*, 1993 Aug, 20(6):773-6.
- [10] O'Tuama LA; Treves ST; Larar JN; Packard AB; Kwan AJ; Barnes PD; Scott RM; Black PM; Madsen JR; Goumnerova LC; et al. Thallium-201 versus technetium-99m-MIBI SPECT in evaluation of childhood brain tumors: a within-subject comparison. *J. Nucl. Med.*, (1993 Jul), 34(7):1045-51.
- [11] D. Aitken, G. Hinkle, M. Thurston, S. Tuttle, D. Martin, J. Olsen, D. Haagensen, D. Houchens, E. Martin, "A Gamma-detecting Probe for Radioimmune Detection of CEA-producing Tumors," *Dis Col & Rect.*, vol. 27, pp. 279-282, 1984.
- [12] H. Barber, H. Barrett, J. Woolfenden, K. Myers, T. Hickernell, "Comparison of in vivo scintillation probes and gamma cameras for detection of small, deep tumors," *Phys Med Biol*, vol. 34, pp. 727-739, 1989.
- [13] O'Dwyer, P.; Mojzisik, C.; Hinkle, G.; Rousseau, M.; Olsen, J.; Tuttle, S.; Barth, R.; Thurston, M.; McCabe, D.; Farrar, W.; Martin, E.: Intraoperative Probe-Directed Immunodetection Using a Monoclonal Antibody. *Arch. Surg*, 121: 1391-1394, 1986.
- [14] H. Reinhardt, H. Meyer, E. Amrein, A Computer-Assisted Device for the Intraoperative CT-Correlated Localization of Brain Tumors," *Eur. Surg. Res.*, Vol. 20, pp. 51-58, 1988.
- [15] B.E. Patt, J.S. Iwanczyk, M.P. Tornai, C.S. Levin, and E.J. Hoffman, "Development of Mercuric Iodide Detector Array for Medical Imaging Applications", *Nucl. Instr. & Meth. in Phys. Res.* A366 (1995) 173-182.
- [16] B.E. Patt, J.S. Iwanczyk, M.P. Tornai, C.S. Levin, and E.J. Hoffman, "Development of A Mercuric Iodide Detector Array for In-Vivo X-Ray Imaging", *Adv. in X-Ray Anal.*, V38. (1995).